



ORIGINAL

Fateh Enouar Mamache · Amar Mesbah · Hanbing Bian ·
Fahmi Zaïri

Micromechanical modeling of the biaxial behavior of strain-induced crystallizable polyethylene terephthalate-clay nanocomposites

Received: 27 February 2022 / Accepted: 6 July 2022 / Published online: 9 August 2022
© The Author(s), under exclusive licence to Springer-Verlag GmbH Germany, part of Springer Nature 2022

Abstract The present work addresses the question of the quantitative prediction of the biaxial response of polymer–clay nanocomposites experiencing strain-induced crystallization. Polyethylene terephthalate is taken as material model to represent the continuous amorphous phase of nanocomposites. A continuum-based micromechanical model is developed to predict the combined effect of strain-induced phase transformation and nanocomposite structural characteristics on the overall elastic-viscoplastic response. Comparisons with available experimental data are presented to illustrate the capabilities of the model in relation to various loading parameters in terms of loading path, loading rate and loading temperature. The model is used to provide a better understanding of the relationship between nanocomposite structural characteristics, phase transformation, intrinsic properties and loading parameters.

Keywords Polymer–clay nanocomposites · Phase transformation · Multiaxial loading · Rate and temperature effects · Micromechanical model

1 Introduction

The adding of clay in a polymer has become a traditional way for producing lightweight nanocomposites. In the latter, the homogeneous dispersion of individual nano-sized clay layers into the matrix material (so-called exfoliated state) constitutes the most favorable situation to optimize the macroscopic properties [1–3]. Compared to their counterpart microcomposites, they present superior chemical/thermal resistance, gas barrier properties and thermo-mechanical properties. Among them, clay-polyethylene terephthalate (PET) nanocomposite systems have several engineering application domains such as food/beverage packaging, gas/liquid containers and flame-retardant systems. The structure–property relationship in PET-clay nanocomposites was investigated in several studies [4–12]. It is now admitted that the continuum-based modeling is helpful for the establishment of the relationship between (nano)structure and mechanical properties of polymer/clay nanocomposites. The reliability of model predictions depends on the utilized method, along with the underlying assumptions, allowing to capture the desired property or the set of properties (i.e., elastic constants, yield and post-yield features). Numerical simulations on 3D/2D material elements were realized in some studies to examine the elastic constants of polymer–clay nanocomposites in connection to the intercalated morphology [13–19]. Analytical models were also proposed to constitutively relate nanocomposite morphology and macroscopic properties

F. E. Mamache · A. Mesbah
Laboratory of Advanced Mechanics, University of Sciences and Technology Houari Boumediene, 16111 Algiers, Algeria

H. Bian · F. Zaïri (✉)
Laboratoire de Génie Civil et géo-Environnement, ULR 4515-LGCgE, Univ. Artois, JUNIA, IMT Nord Europe, Univ. Lille, 59000 Lille, France
e-mail: fahmi.zairi@polytech-lille.fr

[20–33]. In micromechanical constitutive models based on the Eshelby inclusion theory, the constitutive representation consists in discrete spheroids (the clay stacks being represented by an equivalent effective inclusions) randomly dispersed in a continuous polymer matrix. In the latter models, the polymer matrix is assumed to be a rate-independent elastic medium and, at the best, may present plasticity. Nonetheless, a physical consistent constitutive representation should take into account the crystallization process that PET experiences during the mechanical loading. This phase transformation affects the overall mechanical properties and is strongly dependent on the loading parameters in terms of loading level, multiaxial loading, loading rate and loading temperature [34, 35]. The consequence of the clay incorporation on the phase transformation was revealed in very few experimental reports available in the literature [7], but the separate and synergistic effects of structural and loading parameters are difficult to assess experimentally. In order to ensure a reliable design of PET-clay systems, the constitutive model can provide help but should integrate the connection between actual (nano)structure features, loading parameters (temperature, strain rate and loading mode) and phase transformation.

The main purpose of this paper is to develop a modeling for PET-clay nanocomposites based upon the continuum-based micromechanical framework to predict the effect of strain-induced phase transformation and clay nanoparticle characteristics (content, aspect ratio and exfoliated/intercalated state) on the overall elastic-viscoplastic response in relation to the external loading parameters in terms of loading path, loading rate and loading temperature. The model predictability is verified under biaxial loading paths for different temperatures and strain rates.

The outline of this contribution is as follows. Section 2 presents the micromechanics-based constitutive equations. In Sect. 3, the theoretical predictions are compared with available experimental data to verify the capabilities of the present model. Concluding remarks are given in Sect. 4.

2 Micromechanics-based model

2.1 Constitutive equations

The initial two-phase composite becomes a three-phase composite from the onset of phase transformation. The material system is treated as an Eshelby-type inclusion problem in which the representative volume element consists in randomly oriented discrete elastic isotropic spheroids (i.e., the clay particles and the crystals to which we confer the subscripts *clay* and *cry*) randomly dispersed in a continuous elasto-viscoplastic isotropic medium (i.e., the amorphous phase to which we confer the subscript *am*). The three phases are assumed to be perfectly bonded at interfaces.

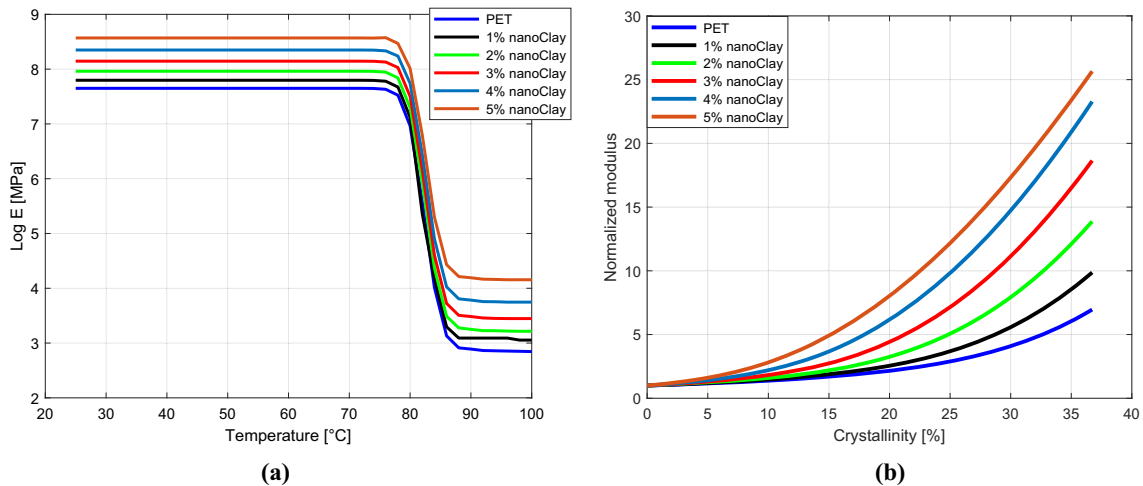


Fig. 1 Stiffness of neat PET and PET-clay systems **a** as a function of temperature and **b** as a function of crystallinity

The Hooke's law constitutively relates the macroscopic stress tensor $\bar{\sigma}$ to the elastic macroscopic strain tensor $\bar{\epsilon}^e$ as follows¹:

$$\bar{\sigma} = \bar{\mathbf{C}} : \bar{\epsilon}^e \tag{1}$$

The macroscopic elastic stiffness tensor $\bar{\mathbf{C}}$ of the multiphase composite is given by [36]:

$$\bar{\mathbf{C}} = \mathbf{C}_{am} \cdot \left\{ \mathbf{I} - (\mathbf{Y}_{clay} + \mathbf{Y}_{cry}) \cdot [(\mathbf{S}_{clay} \cdot \mathbf{Y}_{clay} + \mathbf{S}_{cry} \cdot \mathbf{Y}_{cry}) + \mathbf{I}]^{-1} \right\} \tag{2}$$

where \mathbf{I} is the identity tensor, \mathbf{S}_{clay} and \mathbf{S}_{cry} are the Eshelby tensors and, \mathbf{Y}_{clay} and \mathbf{Y}_{cry} are two fourth-order tensors expressed as:

$$\mathbf{Y}_{clay} = -\phi_{clay} \left[\mathbf{S}_{clay} + (\mathbf{C}_{clay} - \mathbf{C}_{am})^{-1} \cdot \mathbf{C}_{am} \right]^{-1} \quad \text{and} \quad \mathbf{Y}_{cry} = -\phi_{cry} \left[\mathbf{S}_{cry} + (\mathbf{C}_{cry} - \mathbf{C}_{am})^{-1} \cdot \mathbf{C}_{am} \right]^{-1} \tag{3}$$

where ϕ_{clay} is the volume fraction of clay and ϕ_{cry} is the volume fraction of the newly-formed crystals.

The fourth-order isotropic elastic stiffness tensors, \mathbf{C}_{am} , \mathbf{C}_{clay} and \mathbf{C}_{cry} , are expressed, in Cartesian components, as follows:

$$(\mathbf{C}_{am})_{ijkl} = \frac{E_{am}}{2(1 + \nu_{am})} \left[(\delta_{ik}\delta_{jl} + \delta_{il}\delta_{jk}) + \frac{2\nu_{am}}{1 - 2\nu_{am}} \delta_{ij}\delta_{kl} \right] \tag{4}$$

$$(\mathbf{C}_{clay})_{ijkl} = \frac{E_{clay}}{2(1 + \nu_{clay})} \left[(\delta_{ik}\delta_{jl} + \delta_{il}\delta_{jk}) + \frac{2\nu_{clay}}{1 - 2\nu_{clay}} \delta_{ij}\delta_{kl} \right] \tag{5}$$

$$(\mathbf{C}_{cry})_{ijkl} = \frac{E_{cry}}{2(1 + \nu_{cry})} \left[(\delta_{ik}\delta_{jl} + \delta_{il}\delta_{jk}) + \frac{2\nu_{cry}}{1 - 2\nu_{cry}} \delta_{ij}\delta_{kl} \right] \tag{6}$$

in which E_{am} , E_{clay} and E_{cry} are the Young's moduli and, ν_{am} , ν_{clay} and ν_{cry} are the Poisson's ratios. The term δ_{ij} denotes the Kronecker-delta symbol. Note that individual clay platelets exhibit isotropy but intercalated clay stacks present transversal isotropy. The intercalated cluster of clay is replaced by an equivalent particle modeled by an effective (homogeneous) elastic anisotropic spheroid as described in "Appendix A". By this way, the clay structural parameters are integrated, i.e., number of clay layers N , interlayer spacing d_{001} and clay layer dimensions (thickness d_S and length L_S).

The temperature dependence of the amorphous phase is taken into account according to the following function [37]:

$$E_{am}(\theta) = \frac{1}{2}(E_g + E_r) - \frac{1}{2}(E_g - E_r) \tanh\left(\frac{5}{\Delta\theta}(\theta - \theta_g)\right) + X_g(\theta - \theta_g) \tag{7}$$

where E_g is the amorphous modulus in the glassy region, E_r is the amorphous modulus in the rubbery region, $\Delta\theta$ is the interval of the temperature range across which the glass transition occurs and X_g is the slope outside the glass transition region. The variation with temperature θ of the amorphous Poisson's ratio ν_{am} around θ_g is given by the following function:

$$\nu_{am}(\theta) = \nu_g + (\nu_r - \nu_g) \exp\left(\frac{\theta - (2(\theta_g + \Delta\theta) - \theta)}{\theta_g + \Delta\theta}\right)^2 \quad \text{for } \theta < \theta_g \tag{8}$$

$$\nu_{am}(\theta) = \nu_r \quad \text{for } \theta \geq \theta_g \tag{9}$$

where ν_g is the amorphous Poisson's ratio in the glassy region and ν_r is the amorphous Poisson's ratio in the rubbery region.

The macroscopic plastic yielding of the nanocomposite is developed from the continuum plasticity theory. The macroscopic yield surface \bar{F} is expressed as a function of the macroscopic stress $\bar{\sigma}$ and the macroscopic equivalent plastic strain \bar{e}^p as follows [36]:

$$\bar{F} = (1 - \phi_{clay} - \phi_{cry})^2 \bar{\sigma} : (\mathbf{P}^T \cdot \mathbf{B} \cdot \mathbf{P}) : \bar{\sigma} - \frac{2}{3} [\sigma_y + h(\bar{e}^p)^q]^2 \leq 0 \tag{10}$$

¹ The double dot ":" signifies the tensor contraction between a fourth-order tensor and a second-order tensor, while the single dot "." denotes the tensor multiplication between two fourth-order tensors.

in which the von Mises yield criterion with isotropic plastic hardening governs the amorphous plastic yielding where σ_y is the initial yield strength of the amorphous phase and, h and q are the hardening parameters of the amorphous phase. The terms \mathbf{P} and \mathbf{B} are two fourth-order tensors, respectively, written as follows:

$$\mathbf{P} = [\mathbf{I} + (\mathbf{S}_{\text{clay}} - \mathbf{I}) \cdot (\mathbf{Y}_{\text{clay}} + \mathbf{Y}_{\text{cry}})]^{-1} \text{ and } B_{ijkl} = B_{IK}^{(1)} \delta_{ij} \delta_{kl} + B_{IJ}^{(2)} (\delta_{ik} \delta_{jl} + \delta_{il} \delta_{jk}) \quad (11)$$

where $B_{IK}^{(1)}$ and $B_{IJ}^{(2)}$ are given in “Appendix B”. In Eq. (10), \mathbf{P}^T is the transpose of \mathbf{P} .

Regarding the associative plastic flow rule, the macroscopic plastic strain rate $\dot{\bar{\boldsymbol{\epsilon}}}^p$ is obtained from the differentiation of the macroscopic yield function \bar{F} with respect to the macroscopic stress $\bar{\boldsymbol{\sigma}}$:

$$\dot{\bar{\boldsymbol{\epsilon}}}^p = \dot{\lambda} \frac{\partial \bar{F}}{\partial \bar{\boldsymbol{\sigma}}} = 2(1 - \phi_{\text{clay}} - \phi_{\text{cry}})^2 \dot{\lambda} (\mathbf{P}^T \cdot \mathbf{B} \cdot \mathbf{P}) : \bar{\boldsymbol{\sigma}} \quad (12)$$

where $\dot{\lambda}$ is the plastic multiplier computed from the plastic consistency condition: $\dot{\lambda} \langle \dot{\bar{F}} \rangle = 0$, the yield condition being formulated in a Kuhn-Tucker form by: $\dot{\lambda} \geq 0$, $\langle \bar{F} \rangle \leq 0$, $\dot{\lambda} \langle \bar{F} \rangle = 0$.

The macroscopic equivalent plastic strain rate $\dot{\bar{\epsilon}}^p$ is given by:

$$\dot{\bar{\epsilon}}^p = \sqrt{\frac{2}{3} \dot{\bar{\boldsymbol{\epsilon}}}^p : (\mathbf{P}^T \cdot \mathbf{B} \cdot \mathbf{P})^{-1} : \dot{\bar{\boldsymbol{\epsilon}}}^p} = 2(1 - \phi_{\text{clay}} - \phi_{\text{cry}})^2 \dot{\lambda} \sqrt{\frac{2}{3} \bar{\boldsymbol{\sigma}} : (\mathbf{P}^T \cdot \mathbf{B} \cdot \mathbf{P}) : \bar{\boldsymbol{\sigma}}} \quad (13)$$

2.2 Phase transformation

The clay-polymer interactions may provoke the perturbation of the crystallinity. In addition to the nanocomposite structural characteristics, the micromechanical model includes the progressive phase transformation under applied macroscopic deformation. The progressive evolution of crystallization is expressed by an Avrami-type relationship [38, 39]:

$$\phi_{\text{cry}} = \phi_{\infty_{\text{cry}}} \kappa \text{ and } \dot{\kappa} = \frac{\dot{\epsilon}}{\dot{\epsilon}_{\text{ref}}} \alpha_{av} K_{av} (-\ln(1 - \kappa))^{\frac{\alpha_{av}-1}{\alpha_{av}}} (1 - \kappa) \quad (14)$$

in which $\phi_{\infty_{\text{cry}}}$ is the maximum crystal degree, κ is the total degree of transformation, $\dot{\epsilon}$ is the applied strain rate, $\dot{\epsilon}_{\text{ref}}$ is the reference strain rate, α_{av} is the Avrami exponent and K_{av} is the phase transformation rate function defined as follows:

$$K_{av} = 1.47 \times 10^{-3} \left(\frac{4\pi Nu}{3\phi_{\infty_{\text{cry}}}} \right)^{1/3} \exp\left(-\left(\frac{\theta - 141}{47.33}\right)^2\right) \quad (15)$$

in which Nu is the number density of nuclei in the amorphous phase.

The intrinsic viscosity of the amorphous phase is introduced by means of the Duvaut-Lions viscoplastic approach (see “Appendix C”). By this way, the rate-dependency of both the crystallization and the amorphous plastic flow may affect the macroscopic stress.

2.3 Biaxiality effect on intercalation-exfoliation states

Biaxial loading was used in the literature to enhance the exfoliation extent in clay nanocomposites [5, 7]. In our modeling approach, the progressive exfoliation from the original aggregated clay to the completely delaminated one is considered with the following equation:

$$N = \delta N_0 + 1 \quad (16)$$

in which N_0 is the average number of silicate layers per clay stack before mechanical loading and δ is an exfoliation degree parameter expressed as a two-parameter Weibull statistical distribution:

$$\delta = 1 - \exp\left(-\left(\frac{\|\bar{\boldsymbol{\sigma}}\|}{\beta}\right)^\alpha\right) \quad (17)$$

in which α and β are two material parameters and $\|\bar{\boldsymbol{\sigma}}\|$ is the equivalent value of the macroscopic stress tensor $\bar{\boldsymbol{\sigma}}$ for which the components are given under a general biaxial stretching by:

$$\bar{\sigma}_{11} > 0, \bar{\sigma}_{22} = R\bar{\sigma}_{11} \text{ and } \bar{\sigma}_{ij} = 0 \text{ for all other components} \quad (18)$$

where $R = \bar{\sigma}_{22}/\bar{\sigma}_{11}$ is the stress biaxial ratio.

Table 1 Model constants

	Parameter	Significance	Value	Reference
Amorphous phase	E_g	Glassy modulus	2.1 GPa	[40]
	E_r	Rubbery modulus	18 MPa	[41]
	θ_g	Glass transition temperature	77 °C	[42]
	X_g	Transition slope	-0.04 MPa/°C	
	$\Delta\theta$	Temperature shift	10 °C	
	ν_g	Glassy Poisson's ratio	0.35	[42]
	ν_r	Rubbery Poisson's ratio	0.49	[41]
	σ_y	Initial yield strength	3 MPa	
	h	Hardening	4.5 MPa	
	q	Hardening	0.95	
	η	Viscosity	0.01	
Crystalline phase	E_{cry}	Modulus	118 GPa	[43]
	ν_{cry}	Poisson's ratio	0.3	[43]
	α_{cry}	Crystal aspect ratio	2	[44]
	$\dot{\epsilon}_{ref}$	Reference strain-rate	2.1/s	
	α_{av}	Avrami exponent	3	
	Nu	Number density of nuclei	10^8	
Clay	E_{clay}	Modulus	180 GPa	[45]
	ν_{clay}	Poisson's ratio	0.23	[45]
Intercal./exfol. trans	α	Weibull parameter	-0.5	
	β	Weibull parameter	80 MPa	

3 Results

The model parameters are provided in Table 1. The amorphous elastic constants both in the glassy and rubbery states were taken from available data of the literature [40–42]. The crystal elastic constants were taken from the work of Matsuo and Sawatari [43] while the crystal shape factor was obtained from an experimental stiffening curve taken from the work of Cosson et al. [44] on previously crystallized neat PET. Unless otherwise explicitly indicated the clay nanoplatelets were regarded as completely exfoliated with dimensions and elastic constants taken from the molecular dynamics results of Manevitch and Rutledge [45].

3.1 Clay and crystallization reinforcing effect

The model is first used to point out the separate and synergistic effects of clay particles and crystals on the nanocomposite stiffening. Figure 1 presents the impact of the clay loading on the structure-stiffness relationship with temperature variation in amorphous PET (Fig. 1a) or with increase in amount of newly-formed crystals (Fig. 1b). A global view at these plots shows that the increase in clay concentration has a homothetic effect on the modulus variation with temperature in the case of the amorphous PET. Interestingly, the increase in clay concentration amplifies the reinforcing effect in a crystallized PET.

3.2 Comparison with experiments

In what follows, the capabilities of the micromechanics-based model to capture the overall mechanical behavior of PET-based nanocomposites are examined by comparing model simulations to available experimental data [7, 46]. Note that the crystallization in the course of straining was not measured in the work of Shen et al. [7], only the maximum amount was provided. The maximum crystal degree taken from Shen et al. [7] being temperature and rate-dependent, the reduced strain rate $a_\theta \dot{\epsilon}$ is here introduced to plot master curves. Figure 2a shows that when the maximum crystal degree is plotted as a function of the reduced strain rate $a_\theta \dot{\epsilon}$, a straight line fit perfectly describes the experimental data of both neat PET and its nanocomposite.

3.2.1 Neat PET

The material constants for the neat PET were the outcome of a standard optimization procedure that provides the best fit of the uniaxial crystallization data of Salem [41] and the equal biaxial stress-strain data of Shen

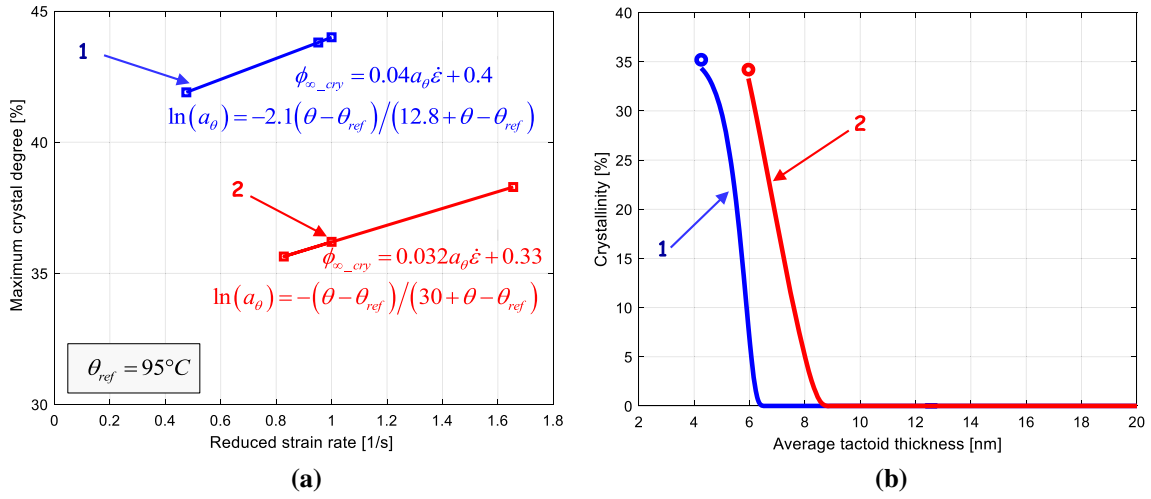


Fig. 2 Maximum crystal degree as a function of **a** reduced strain rate $a_{\theta}\dot{\epsilon}$ (1: neat PET and 2: PET-clay system at 6% wt. clay), **b** average tactoid thickness (1: 95 °C and 1/s, 2: 102 °C and 1/s); Solid lines: model; Symbols: experimental data of Shen et al. [7]

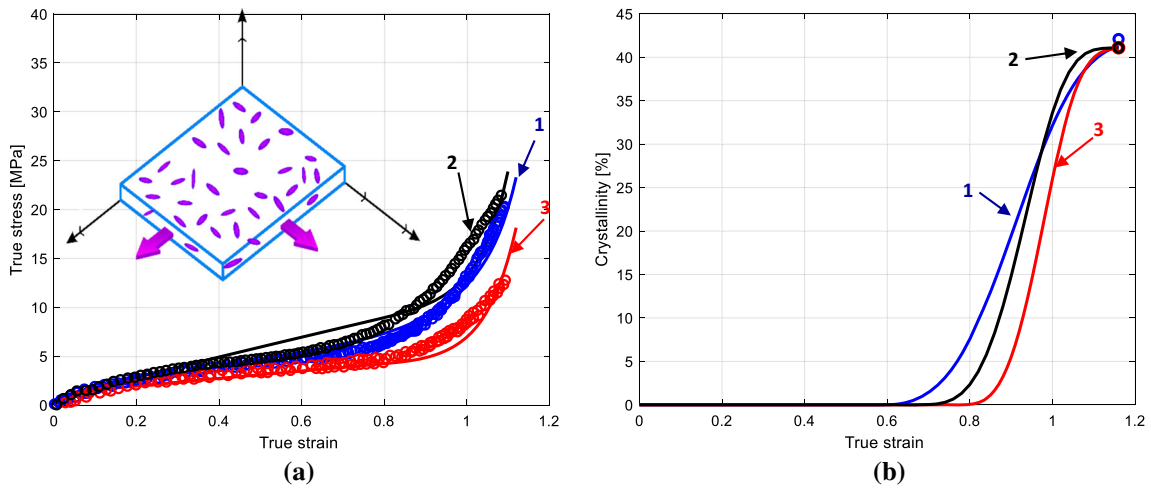


Fig. 3 Model results for neat PET under EB loading at different loading conditions (1: 95 °C and 1/s, 2: 102 °C and 2/s, 3: 102 °C and 1/s); **a** stress–strain response, **b** strain-induced crystallization; Solid lines: model; Symbols: experimental data of Shen et al. [7]

et al. [7]. Figure 3 presents the model results in comparison with Shen et al. [7] data for different strain rates and temperatures. The different features of the stress–strain response are satisfactory captured by the model, including the initial linear elasticity, the yield strength and the post-yield behavior. As expected, the maximum crystal amount is perfectly caught by the model.

3.2.2 PET-clay nanocomposite

Figure 4 presents the equal biaxial (EB) response of a PET-based nanocomposite system for different strain rates and temperatures. The model reproduces adequately the important effect of the loading parameters on the mechanical response. Especially, the delay in the onset of strain stiffening due to the temperature increase or the strain rate decrease. Again, the maximum crystal amount is satisfactory reproduced by the model. The PET-clay system having a lower crystallinity than the neat PET, the model is then found able to capture the crystallization reduction due to a confinement effect related to the restriction in mobility of the polymer chains trapped between the clay layers. The model is therefore able to connect both the clay structural characteristics and the phase transformation with the macroscopic behavior.

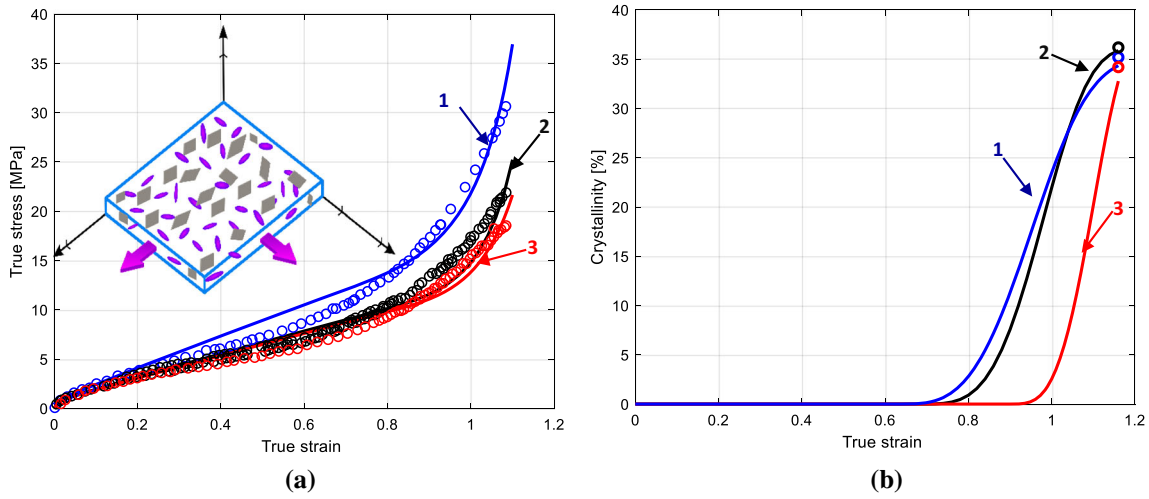


Fig. 4 Model results for a PET-clay system (6% wt. clay) under EB loading at different loading conditions (1: 95 °C and 1/s, 2: 102 °C and 2/s, 3: 102 °C and 1/s): **a** stress–strain response, **b** strain-induced crystallization; Solid lines: model; Symbols: experimental data of Shen et al. [7]

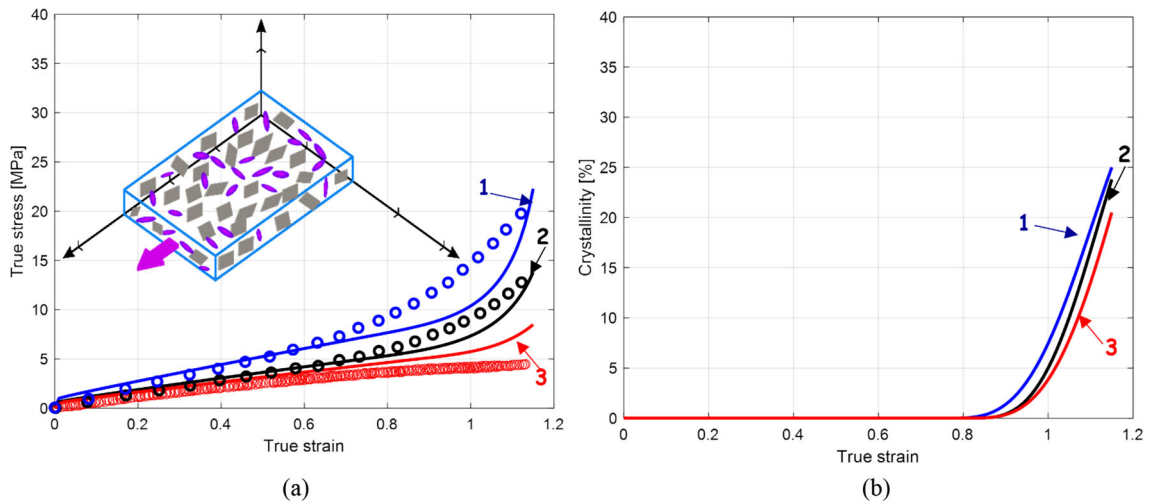


Fig. 5 Model results for neat PET and PET-clay systems (1: 2.5% wt. clay, 2: 1% wt. clay, 3: neat PET) under CW loading at 100 °C and 1/s: **a** stress–strain response, **b** strain-induced crystallization; Solid lines: model; Symbols: experimental data of Figiel et al. [46]

Figure 5 presents model predictions under constant width (CW) condition in comparison of experimental data of Figiel et al. [46] for neat PET and two of its nanocomposites.

The clay content effect on the plastic flow response is adequately reproduced by the model, especially the reinforcing effect on the strain hardening ability. It can be also observed that the incubation strain, below which no phase transformation is detected, decreases when the clay loading increases. The model can be used to predict the stress–crystallinity evolution in response to a temperature change. Illustrative examples of the EB material response are presented in Figs. 6 and 7 for the neat PET and its nanocomposite, respectively, for two successive temperatures: 102 °C and 95 °C. The simulation consists to an isothermal straining at 102 °C up to a pre-determined strain level, then a progressive cooling is performed at a constant rate until a temperature of 95 °C. The isothermal stress response and phase transformation at 102 °C and 95 °C are also presented in the figure.

As a final point of discussion, the model ability to relate structural state, overall response and loading parameters is shown. Figure 8 shows the model prediction under EB stretching at two stretching temperatures considering intercalated morphology, exfoliated morphology and strain-induced intercalated-exfoliated morphology transformation.

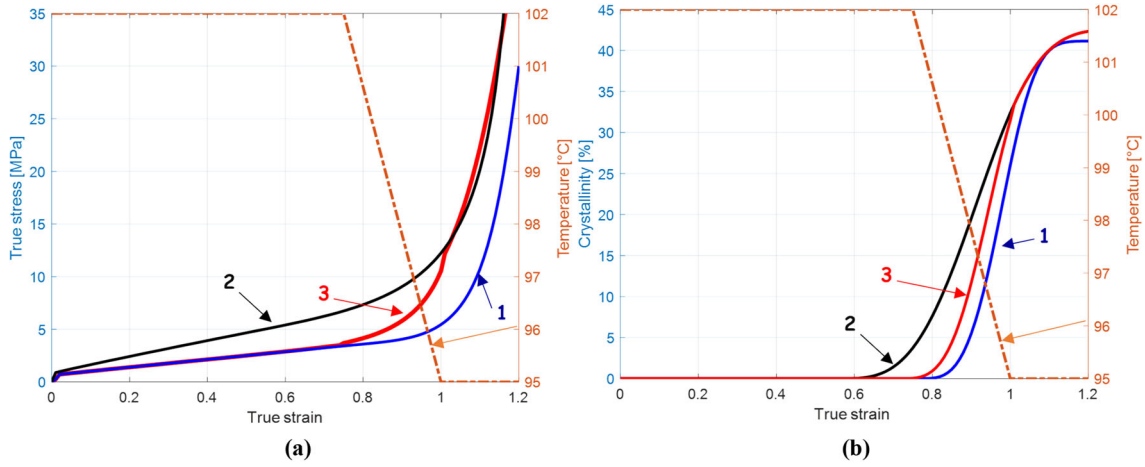


Fig. 6 Model results for neat PET considering two temperature levels under EB loading at 1/s (1: 102 °C, 2: 95 °C, 3: 102 °C and then 95 °C)

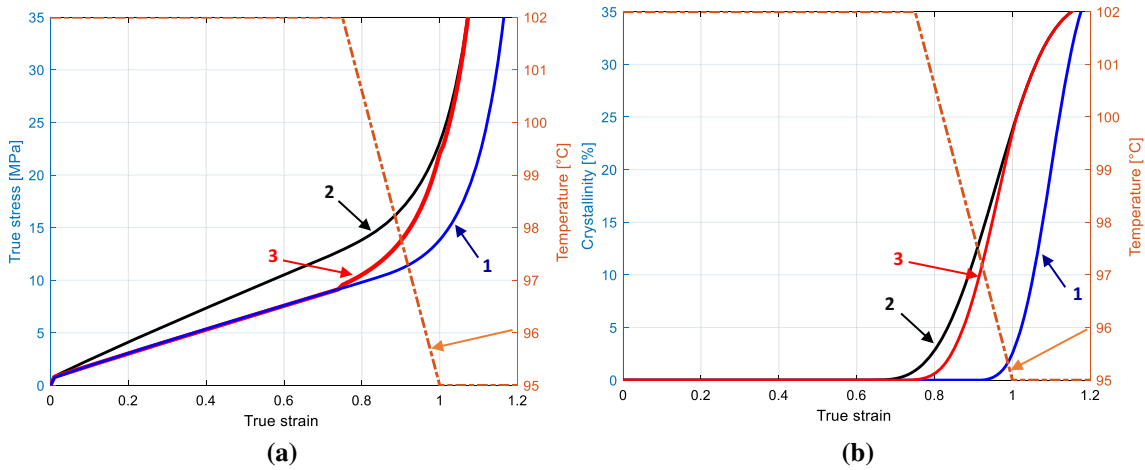


Fig. 7 Model results for a PET-clay system (6% wt. clay) considering two temperature levels under EB loading at 1/s (1: 102 °C, 2: 95 °C, 3: 102 °C and then 95 °C)

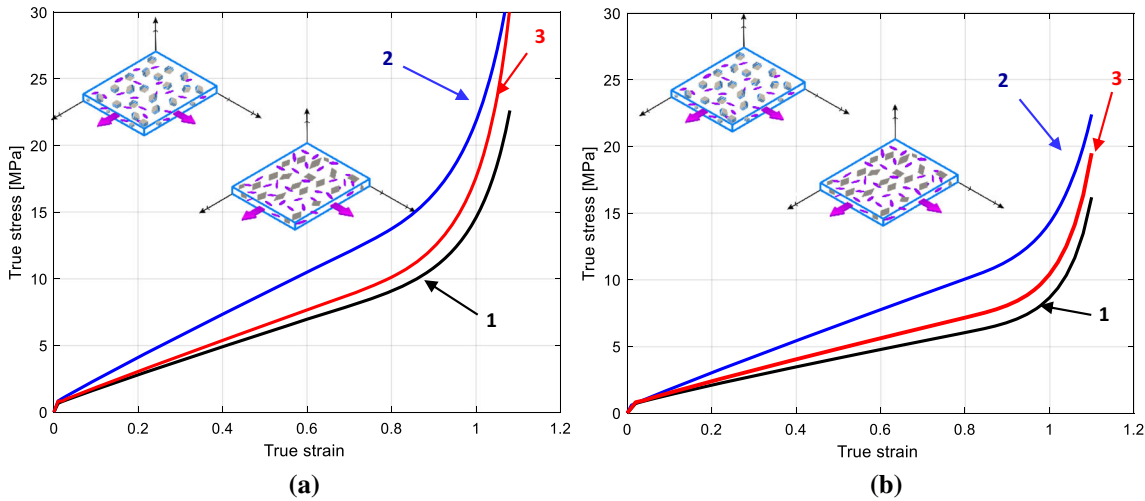


Fig. 8 Model results for a PET-clay system (6% wt. clay) under EB loading considering different morphology states (1: intercalated morphology, 2: exfoliated morphology, 3: strain-induced intercalated-exfoliated morphology transformation): **a** 95 °C and 1/s, **b** 102 °C and 1/s

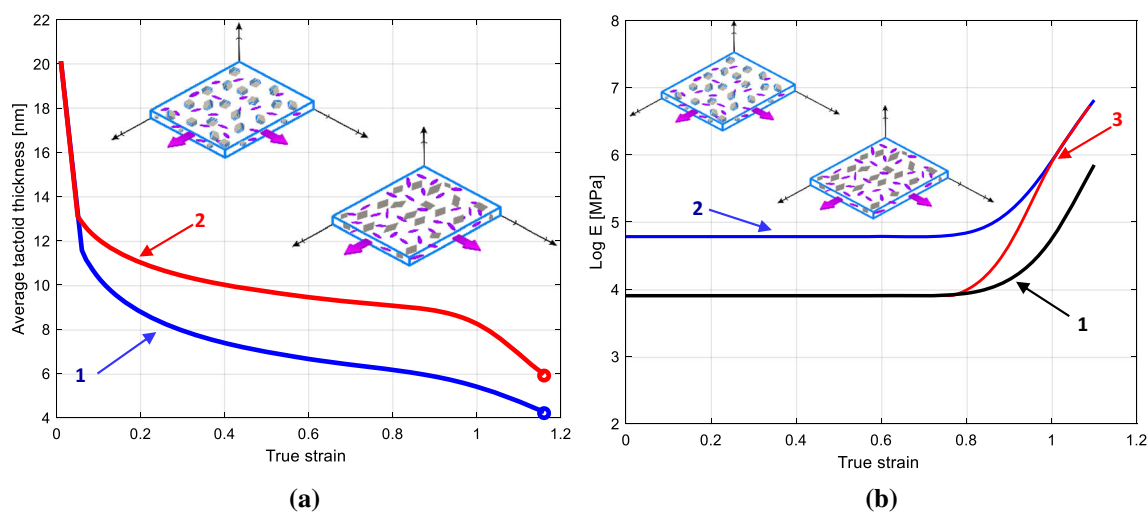


Fig. 9 Model results for a PET-clay system (6% wt. clay) on the EB loading effect on **a** the average thickness of the intercalated clay stack (1: 95 °C and 1/s, 2: 102 °C and 1/s), **b** the stiffening considering different morphology states (1: intercalated morphology, 2: exfoliated morphology, 3: strain-induced intercalated-exfoliated morphology transformation)

As expected intercalated and exfoliated states lead to lower and upper bound model predictions, respectively, between which the experimental data of Shen et al. [7] fall. The degree of exfoliation may be increased by the biaxial stretching caused by the delamination of the intercalated layers [5, 7]. The model results may be then better favorably compared to the experimental data when an evolution from intercalation to exfoliation states caused by the EB loading is introduced. The EB stretching improves the exfoliation as the average tactoid thickness diminishes in the course of the loading. The split of the large tactoids into thinner and smaller tactoids is significantly influenced by the stretching temperature as illustrated in Fig. 9a, the better delamination of tactoids at the lowest stretching temperature leading to the hardening ability enhancement due to the new exfoliated state. The correlation between crystallinity rate and exfoliated clay is observed in Fig. 2b. The decrease in the tactoid thickness with the EB stretching produces an increase in crystal degree due to the decrease in confinement effect on the crystallization of the polymer chains. The combined effect of strain-induced nanocomposite structural evolution and strain-induced phase transformation leads to the enhanced stiffening as illustrated in Fig. 9b.

4 Concluding remarks

In this paper, the strain-induced crystallization was incorporated into an elastic-viscoplastic micromechanical constitutive representation of the PET-clay nanocomposite. The model-experiments comparisons demonstrated the capability of the model to describe the biaxial elastic-viscoplastic response of neat PET and its nanocomposites under different loading conditions in terms of strain rate and temperature. The model provides a useful tool to tailor and optimize the microstructure-property relationship of strain-induced crystallizable PET-clay nanocomposites. Separate and synergistic effects of nanocomposite structural characteristics, phase transformation and loading parameters on the overall response were highlighted thanks to the model.

Declarations

Conflict of interest The authors declare that they have no conflict of interest.

Appendix A

The intercalated cluster of clay is replaced by an equivalent homogeneous nanoparticle having transversely isotropic properties. Each intercalated clay stack is seen as a laminated composite sub-structure, consisting of

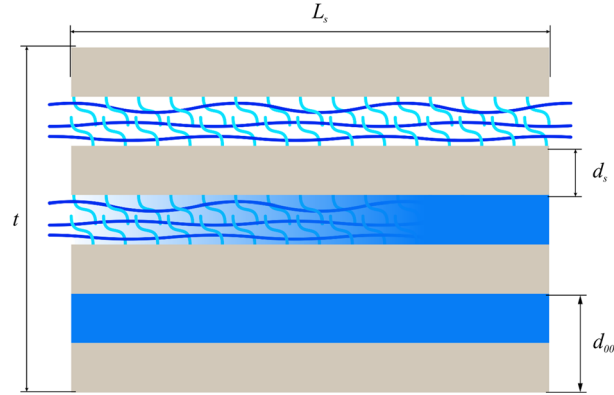


Fig. 10 Intercalated clay stack

several clay platelets separated by polymer, for which the elastic tensor is estimated using the laminate theory [30]. The elastic stiffness tensor \mathbf{C}_{clay} is given from the six elastic constants written as:

$$\begin{aligned}
 E_{11} &= E_{33} = \phi_{S/P} E_S + (1 - \phi_{S/P}) E_G \\
 E_{22} &= \frac{E_S E_G}{\phi_{S/P} E_G + (1 - \phi_{S/P}) E_S - \phi_{S/P} (1 - \phi_{S/P}) \eta_1 E_G E_S} \\
 \nu_{12} &= \nu_{23} = \phi_{S/P} \nu_S + (1 - \phi_{S/P}) \nu_G \\
 \nu_{13} &= \frac{\nu_S \phi_{S/P} E_S (1 - \nu_G^2) + \nu_G (1 - \phi_{S/P}) E_G (1 - \nu_S^2)}{\phi_{S/P} E_S (1 - \nu_G^2) + \nu_G (1 - \phi_{S/P}) E_G (1 - \nu_S^2)} \\
 G_{12} &= G_{23} = \frac{G_S G_G}{\phi_{S/P} G_G + (1 - \phi_{S/P}) G_S - \phi_{S/P} (1 - \phi_{S/P}) \eta_2 G_G G_S} \\
 G_{13} &= \frac{E_{11}}{2(1 + \nu_{13})}
 \end{aligned} \tag{A1}$$

The two parameters η_1 and η_2 are given by:

$$\begin{aligned}
 \eta_1 &= \frac{\nu_S^2 E_G / E_S + \nu_G^2 E_S / E_G - 2\nu_S \nu_G}{\phi_{S/P} E_S + (1 - \phi_{S/P}) E_G} \\
 \eta_2 &= \frac{\nu_S^2 G_G / G_S + \nu_G^2 G_S / G_G - 2\nu_S \nu_G}{\phi_{S/P} G_S + (1 - \phi_{S/P}) G_G}
 \end{aligned} \tag{A2}$$

where E is the Young's modulus, G is the shear modulus and ν is the Poisson's ratio. The subscripts S and G refer to the silicate and the gallery (confined polymer matrix in the intersilicate layers whose elastic constants are taken equal to those of the amorphous PET), respectively. The term $\phi_{S/P}$ is the volume fraction of silicate in the intercalated clay stack:

$$\phi_{S/P} = \frac{N d_S}{t} \tag{A3}$$

where t is the thickness of the intercalated clay stack:

$$t = (N - 1) d_{001} + d_S \tag{A4}$$

The quantities N , d_{001} and d_S are the clay structural parameters schematically defined in Fig. 10. They denote, respectively, the average number of silicate layers per clay stack, the average silicate interlayer spacing and the thickness of the silicate layer, respectively. When the intercalated morphology is invoked in the main body of the paper, the employed average structural parameters are $N = 8$, $L_S = 200$ nm, $d_S = 1$ nm and $d_{001} = 2$ nm.

The volume fraction of intercalated clay stacks can be expressed as:

$$\phi_{\text{clay}} = \frac{\rho_m}{\rho_S \phi_{S/P}} W_S \tag{A5}$$

where W_S is the silicate weight fraction, ρ_S is the silicate density and ρ_m is the density of the polymer matrix:

$$\rho_m = \phi_{\text{am}} \rho_{\text{am}} + \phi_{\text{cry}} \rho_{\text{cry}} \tag{A6}$$

The PET, crystal and clay densities were taken equal to 1.335 g/cm³, 1.445 g/cm³ and 2.3 g/cm³, respectively.

The aspect ratio of the intercalated clay stack α_{clay} is given by:

$$\alpha_{\text{clay}} = \frac{(N - 1)d_{001} + d_S}{L_S} \tag{A7}$$

where L_S is the clay layer length.

The crystal volume fraction ϕ_{cry} is calculated from the crystal weight fraction W_{cry} as follows:

$$\phi_{\text{cry}} = \frac{W_{\text{cry}}}{W_{\text{cry}} + \left(\frac{\rho_{\text{cry}}}{\phi_{\text{am}} \rho_{\text{am}} + \phi_{\text{clay}} \rho_{\text{clay}}} \right) (1 - W_{\text{cry}})} \tag{A8}$$

Appendix B

The parameters $B_{IK}^{(1)}$ and $B_{IJ}^{(2)}$ are given by:

$$B_{IK}^{(1)} = -\frac{1}{3} + \frac{2}{4725(1 - \nu_{\text{am}})^2} \left\{ \begin{aligned} & \left[\begin{aligned} & 3(35\nu_{\text{am}}^2 - 70\nu_{\text{am}} + 36)\Delta_{IK} \\ & + 7(50\nu_{\text{am}}^2 - 59\nu_{\text{am}} + 8)(\Delta_I + \Delta_K) \\ & - 2(175\nu_{\text{am}}^2 - 343\nu_{\text{am}} + 103) \end{aligned} \right] \left(\frac{\phi_{\text{clay}}}{D_{II}D_{KK}} + \frac{\phi_{\text{cry}}}{E_{II}E_{KK}} \right) \\ & + 21(25\nu_{\text{am}} - 2)(1 - 2\nu_{\text{am}}) \left(\frac{\phi_{\text{clay}}}{\phi_{\text{cry}}} \frac{(G_{II} + G_{KK})}{\frac{D_{II}D_{KK}}{(H_{II} + H_{KK})}} \right) \\ & + 21(25\nu_{\text{am}} - 23)(1 - 2\nu_{\text{am}}) \left(\frac{\phi_{\text{clay}}}{\phi_{\text{cry}}} \frac{(G_{II}\Delta_K + G_{KK}\Delta_I)}{\frac{D_{II}D_{KK}}{(H_{II}\Delta_K + H_{KK}\Delta_I)}} \right) \\ & + 1575(1 - 2\nu_{\text{am}})^2 \left(\phi_{\text{clay}} \frac{G_{II}G_{KK}}{D_{II}D_{KK}} + \phi_{\text{cry}} \frac{H_{II}H_{KK}}{E_{II}E_{KK}} \right) \end{aligned} \right\} \tag{B1}$$

$$B_{IJ}^{(2)} = \frac{1}{2} + \frac{1}{1575(1 - \nu_{\text{am}})^2} \left(\frac{\phi_{\text{clay}}}{D_{IJ}D_{IJ}} + \frac{\phi_{\text{cry}}}{E_{IJ}E_{IJ}} \right) \left[\begin{aligned} & (70\nu_{\text{am}}^2 - 140\nu_{\text{am}} + 72)\Delta_{IJ} \\ & - (175\nu_{\text{am}}^2 - 266\nu_{\text{am}} + 75) \frac{(\Delta_I + \Delta_J)}{2} \\ & + (350\nu_{\text{am}}^2 - 476\nu_{\text{am}} + 164) \end{aligned} \right]$$

where $\Delta_I, \Delta_{IJ}, D_{IJ}, E_{IJ}, G_{IJ}$ and H_{IJ} are defined by:

$$\Delta_1 = \frac{3[1 - \alpha^4 g(\alpha^2)]}{1 - \alpha^4},$$

$$\Delta_2 = \Delta_3 = \frac{1}{2}(3 - \Delta_1),$$

$$\begin{aligned}\Delta_{11} &= \frac{5[2 + \alpha^4 - 3\alpha^4 g(\alpha^2)]}{2(1 - \alpha^4)^2}, \\ \Delta_{12} = \Delta_{21} = \Delta_{13} = \Delta_{31} &= \frac{15\alpha^4[-3 + (1 + 2\alpha^4)g(\alpha^2)]}{4(1 - \alpha^4)^2}, \\ \Delta_{22} = \Delta_{23} = \Delta_{32} = \Delta_{33} &= \frac{1}{8}(15 - 3\Delta_{11} - 4\Delta_{12})\end{aligned}\quad (\text{B2})$$

with

$$g(\alpha) = \begin{cases} \frac{\cosh^{-1} \alpha}{\alpha\sqrt{\alpha^2 - 1}} & \text{if } \alpha > 1 \\ \frac{\cos^{-1} \alpha}{\alpha\sqrt{1 - \alpha^2}} & \text{if } \alpha < 1 \end{cases} \quad (\text{B3})$$

$$D_{IJ} = 2(V_{IJ} + NP_{IJ})$$

$$E_{IJ} = 2(V_{IJ} + NI_{IJ}) \quad (\text{B4})$$

and

$$\begin{aligned}\begin{Bmatrix} G_{I1} \\ G_{I2} \\ G_{I3} \end{Bmatrix} &= \begin{bmatrix} U_{11} + 2V_{11} + WP_{11} & U_{21} + MP_{21} & U_{31} + MP_{31} \\ U_{12} + MP_{12} & U_{22} + 2V_{22} + \bar{W}P_{22} & U_{32} + MP_{32} \\ U_{13} + MP_{13} & U_{23} + MP_{23} & U_{33} + 2V_{33} + \bar{W}P_{33} \end{bmatrix}^{-1} \begin{Bmatrix} U_{11} + MP_{I1} \\ U_{12} + MP_{I2} \\ U_{13} + MP_{I3} \end{Bmatrix} \\ \begin{Bmatrix} H_{I1} \\ H_{I2} \\ H_{I3} \end{Bmatrix} &= \begin{bmatrix} U_{11} + 2V_{11} + WI_{11} & U_{21} + MI_{21} & U_{31} + MI_{31} \\ U_{12} + MI_{12} & U_{22} + 2V_{22} + \bar{W}I_{22} & U_{32} + MI_{32} \\ U_{13} + MI_{13} & U_{23} + MI_{23} & U_{33} + 2V_{33} + \bar{W}I_{33} \end{bmatrix}^{-1} \begin{Bmatrix} U_{11} + MI_{I1} \\ U_{12} + MI_{I2} \\ U_{13} + MI_{I3} \end{Bmatrix}\end{aligned}\quad (\text{B5})$$

with

$$\begin{aligned}U_{11} &= \left(4\nu_{\text{am}} + \frac{2}{\alpha^2 - 1}\right)f(\alpha) + 4\nu_{\text{am}} + \frac{4}{3(\alpha^2 - 1)}, \\ U_{12} = U_{13} &= \left(4\nu_{\text{am}} - \frac{2\alpha^2 + 1}{\alpha^2 - 1}\right)f(\alpha) + 4\nu_{\text{am}} - \frac{2\alpha^2}{\alpha^2 - 1}, \\ U_{21} = U_{31} &= \left(-2\nu_{\text{am}} - \frac{2\alpha^2 + 1}{\alpha^2 - 1}\right)f(\alpha) - \frac{2\alpha^2}{\alpha^2 - 1}, \\ U_{22} = U_{23} = U_{32} = U_{33} &= \left(-2\nu_{\text{am}} + \frac{4\alpha^2 - 1}{4(\alpha^2 - 1)}\right)f(\alpha) + \frac{\alpha^2}{2(\alpha^2 - 1)},\end{aligned}\quad (\text{B6})$$

$$\begin{aligned}V_{11} &= \left(-4\nu_{\text{am}} + \frac{4\alpha^2 - 2}{\alpha^2 - 1}\right)f(\alpha) - 4\nu_{\text{am}} + \frac{12\alpha^2 - 8}{3(\alpha^2 - 1)}, \\ V_{12} = V_{21} = V_{13} = V_{31} &= \left(-\nu_{\text{am}} - \frac{\alpha^2 + 2}{\alpha^2 - 1}\right)f(\alpha) - 2\nu_{\text{am}} - \frac{2}{\alpha^2 - 1}, \\ V_{22} = V_{23} = V_{32} = V_{33} &= \left(2\nu_{\text{am}} - \frac{4\alpha^2 - 7}{4(\alpha^2 - 1)}\right)f(\alpha) + \frac{\alpha^2}{2(\alpha^2 - 1)},\end{aligned}\quad (\text{B7})$$

$$MP_{IJ} = \frac{\lambda_{\text{am}}\mu_{\text{clay}} - \lambda_{\text{clay}}\mu_{\text{am}}}{(\mu_{\text{clay}} - \mu_{\text{am}})[2(\mu_{\text{clay}} - \mu_{\text{am}}) + 3(\lambda_{\text{clay}} - \lambda_{\text{am}})]},$$

$$NP_{IJ} = \frac{\mu_{\text{am}}}{2(\mu_{\text{clay}} - \mu_{\text{am}})},$$

$$MI_{IJ} = \frac{\lambda_{\text{am}}(1 - \Omega_{IK}^{(i)}\delta_{kk}) - 2\mu_{\text{am}}\Omega_{IJ}^{(i)}}{2(\mu_{\text{cry}} - \mu_{\text{am}})},$$

$$\begin{aligned}
 N_{IJ} &= \frac{\mu_{am}}{2(\mu_{cry} - \mu_{am})}, \\
 WP_{II} &= MP_{II} + 2NP_{II}, \\
 WI_{II} &= MI_{II} + 2NI_{II}.
 \end{aligned}
 \tag{B8}$$

in which λ and μ are the Lamé's constants and

$$\begin{Bmatrix} \Omega_{I1} \\ \Omega_{I2} \\ \Omega_{I3} \end{Bmatrix} = \begin{bmatrix} \gamma & \lambda_{cry} - \lambda_{am} & \lambda_{cry} - \lambda_{am} \\ \lambda_{cry} - \lambda_{am} & \gamma & \lambda_{cry} - \lambda_{am} \\ \lambda_{cry} - \lambda_{am} & \lambda_{cry} - \lambda_{am} & \gamma \end{bmatrix}^{-1} \begin{Bmatrix} \lambda_{cry} - \lambda_{am} \\ \lambda_{cry} - \lambda_{am} \\ \lambda_{cry} - \lambda_{am} \end{Bmatrix}
 \tag{B9}$$

with $\gamma = \lambda_{cry} - \lambda_{am} + 2(\mu_{cry} - \mu_{am})$.

Appendix C

The Duvaut-Lions approach was employed to transform plasticity to viscoplasticity [47, 48]:

$$\dot{\mathbf{e}}^{vp} = \frac{1}{\eta} \mathbf{C}_{am}^{-1} : (\bar{\boldsymbol{\sigma}} - \bar{\bar{\boldsymbol{\sigma}}})
 \tag{C1}$$

$$\dot{\mathbf{e}}^{vp} = \frac{1}{\eta} (\bar{\mathbf{e}}^{vp} - \bar{\bar{\mathbf{e}}}^p)
 \tag{C2}$$

where η is a viscosity parameter, $\bar{\boldsymbol{\sigma}}$ and $\bar{\bar{\boldsymbol{\sigma}}}$ are the total average viscoplastic stress tensor and the overall inviscid plastic stress tensor, respectively, and, $\bar{\mathbf{e}}^{vp}$ and $\bar{\bar{\mathbf{e}}}^p$ are the viscoplastic strain tensor and the inviscid plastic strain tensor, respectively. The inviscid solution, in terms of the actual stress tensor $\bar{\bar{\boldsymbol{\sigma}}}_{n+1}$ and the internal variable $\bar{\bar{\mathbf{e}}}_{n+1}^p$, is updated at each increment allowing the calculation of the new stress $\bar{\boldsymbol{\sigma}}_{n+1}$ and the viscoplastic strain $\bar{\mathbf{e}}_{n+1}^{vp}$ by integrating the two previous equations using a backward Euler algorithm:

$$\bar{\boldsymbol{\sigma}}_{n+1} = \frac{(\bar{\boldsymbol{\sigma}}_n + \mathbf{C}_{am} : \Delta \bar{\mathbf{e}}_{n+1}) + \frac{\Delta t_{n+1}}{\eta} \bar{\bar{\boldsymbol{\sigma}}}_{n+1}}{1 + \frac{\Delta t_{n+1}}{\eta}}
 \tag{C3}$$

$$\bar{\mathbf{e}}_{n+1}^{vp} = \frac{\bar{\mathbf{e}}_n^{vp} + \frac{\Delta t_{n+1}}{\eta} \bar{\bar{\mathbf{e}}}_{n+1}^p}{1 + \frac{\Delta t_{n+1}}{\eta}}
 \tag{C4}$$

where Δt_{n+1} is the time step. When $\Delta t_{n+1}/\eta \rightarrow \infty$ the inviscid solution is recovered and when $\Delta t_{n+1}/\eta \rightarrow 0$ the elastic solution is achieved.

References

1. Kojima, Y., Usuki, A., Kawasumi, M., Okada, A., Fukushima, Y., Kurauchi, T., Kamigaito, O.: Mechanical properties of nylon 6-clay hybrid. *J. Mater. Res.* **8**, 1185–1189 (1993)
2. Usuki, A., Kojima, Y., Kawasumi, M., Okada, A., Fukushima, Y., Kurauchi, T., Kamigaito, O.: Synthesis of nylon 6-clay hybrid. *J. Mater. Res.* **8**, 1179–1184 (1993)
3. Pavlidou, S., Papaspyrides, C.D.: A review on polymer-layered silicate nanocomposites. *Prog. Polym. Sci.* **33**, 1119–1198 (2008)
4. Ke, Y., Long, C., Qi, Z.: Crystallization, properties, and crystal and nanoscale morphology of PET-clay nanocomposites. *J. Appl. Polym. Sci.* **71**, 1139–1146 (1999)
5. Rajeev, R.S., Harkin-Jones, E., Soon, K., McNally, T., Menary, G., Armstrong, C.G., Martin, P.J.: Studies on the effect of equi-biaxial stretching on the exfoliation of nanoclays in polyethylene terephthalate. *Eur. Polym. J.* **45**, 332–340 (2009)
6. Alongi, J., Frache, A., Gioffredi, E.: Fire-retardant poly(ethylene terephthalate) by combination of expandable graphite and layered clays for plastics and textiles. *Fire Mater.* **35**, 383–396 (2011)
7. Shen, Y., Harkin-Jones, E., Hornsby, P., McNally, T., Abu-Zurayk, R.: The effect of temperature and strain rate on the deformation behaviour, structure development and properties of biaxially stretched PET-clay nanocomposites. *Compos. Sci. Technol.* **71**, 758–764 (2011)
8. Wang, Y., Jabarin, S.A.: Novel preparation method for enhancing nanoparticle dispersion and barrier properties of poly(ethylene terephthalate) and poly(m-xylylene adipamide). *J. Appl. Polym. Sci.* **129**, 1455–1465 (2013)

9. Wu, J.H., Yen, M.S., Kuo, M.C., Wu, C.P., Leu, M.T., Li, C.H., Tsai, F.K.: Poly(ethylene terephthalate)/poly(ethylene glycol-co-1,3/1,4-cyclohexanedimethanol terephthalate)/clay nanocomposites: morphology and isothermal crystallization kinetics. *J. Appl. Polym. Sci.* **128**, 487–497 (2013)
10. Dini, M., Mousavand, T., Carreau, J.P., Kamal, R.M., Ton-That, M.T.: Microstructure and properties of poly(ethylene terephthalate)/organoclay nanocomposites prepared by water-assisted extrusion: effect of organoclay concentration. *Polym. Eng. Sci.* **54**, 1879–1892 (2014)
11. Korivi, N.S.: Preparation, characterization, and applications of poly(ethylene terephthalate) nanocomposites. In: *Manufacturing of Nanocomposites with Engineering Plastics*, pp. 167–198 (2015).
12. Saxena, D., Rana, D., Bhoje Gowd, E., Maiti, P.: Improvement in mechanical and structural properties of poly(ethylene terephthalate) nanohybrid. *SN Appl. Sci.* **1**, 1363 (2019)
13. Hbaieb, K., Wang, Q.X., Chia, Y.H.J., Cotterell, B.: Modelling stiffness of polymer/clay nanocomposites. *Polymer* **48**, 901–909 (2007)
14. Figiel, L., Buckley, C.P.: Elastic constants for an intercalated layered-silicate/polymer nanocomposite using the effective particle concept - A parametric study using numerical and analytical continuum approaches. *Comput. Mater. Sci.* **44**, 1332–1343 (2009)
15. Pahlavanpour, M., Moussaddy, H., Ghossein, E., Hubert, P., Lévesque, M.: Prediction of elastic properties in polymer-clay nanocomposites: analytical homogenization methods and 3D finite element modeling. *Comput. Mater. Sci.* **79**, 206–215 (2013)
16. Pisano, C., Figiel, L.: Modelling of morphology evolution and macroscopic behaviour of intercalated PET-clay nanocomposites during semi-solid state processing. *Compos. Sci. Technol.* **75**, 35–41 (2013)
17. Figiel, L.: Effect of the interphase on large deformation behaviour of polymer-clay nanocomposites near the glass transition: 2D RVE computational modelling. *Comput. Mater. Sci.* **84**, 244–254 (2014)
18. Figiel, L.: Nonlinear multiscale modelling of quasi-solid state behaviour of PET/MWCNT nanocomposites: 3D RVE-based approach. *Composites Communications* **8**, 101–105 (2018)
19. Vo, V.S., Nguyen, V.H., Chergui, M.S., Benjamin, C., Salah, N.: Estimation of effective elastic properties of polymer/clay nanocomposites: a parametric study. *Compos. B Eng.* **152**, 139–150 (2018)
20. Brune, D.A., Bicerano, J.: Micromechanics of nanocomposites: comparison of tensile and compressive elastic moduli, and prediction of the effects of incomplete exfoliation and imperfect alignment on modulus. *Polymer* **43**, 369–387 (2002)
21. Ji, X.L., Jing, J.K., Jiang, W., Jiang, B.Z.: Tensile modulus of polymer nanocomposites. *Polym. Eng. Sci.* **42**, 983–993 (2002)
22. Fornes, T.D., Paul, D.R.: Modeling properties of nylon 6/clay nanocomposites using composite theories. *Polymer* **44**, 4993–5013 (2003)
23. Luo, J.J., Daniel, I.M.: Characterization and modeling of mechanical behavior of polymer/clay nanocomposites. *Compos. Sci. Technol.* **63**, 1607–1616 (2003)
24. Sheng, N., Boyce, M.C., Parks, D.M., Rutledge, G.C., Abes, J.I., Cohen, R.C.: Multiscale micromechanical modeling of polymer/clay nanocomposites and the effective clay particle. *Polymer* **45**, 487–506 (2004)
25. Wang, J., Pyrz, R.: Prediction of the overall moduli of layered silicate-reinforced nanocomposites-part I: basic theory and formulas. *Compos. Sci. Technol.* **64**, 925–934 (2004)
26. Anthoulis, G.I., Kontou, E.: Micromechanical behaviour of particulate polymer nanocomposites. *Polymer* **49**, 1934–1942 (2008)
27. Mesbah, A., Zaïri, F., Boutaleb, S., Gloaguen, J.M., Naït-Abdelaziz, M., Xie, S., Boukharouba, T., Lefebvre, J.M.: Experimental characterization and modeling stiffness of polymer/clay nanocomposites within a hierarchical multiscale framework. *J. Appl. Polym. Sci.* **114**, 3274–3291 (2009)
28. Anoukou, K., Zaïri, F., Naït-Abdelaziz, M., Zaoui, A., Messenger, T., Gloaguen, J.M.: On the overall elastic moduli of polymer-clay nanocomposite materials using a self-consistent approach. Part I: Theory. *Compos. Sci. Technol.* **71**, 197–205 (2011)
29. Anoukou, K., Zaïri, F., Naït-Abdelaziz, M., Zaoui, A., Messenger, T., Gloaguen, J.M.: On the overall elastic moduli of polymer-clay nanocomposite materials using a self-consistent approach. Part II: Experimental verification. *Compos. Sci. Technol.* **71**, 206–215 (2011)
30. Zaïri, F., Gloaguen, J.M., Naït-Abdelaziz, M., Mesbah, A., Lefebvre, J.M.: Study of the effect of size and clay structural parameters on the yield and post-yield response of polymer/clay nanocomposites via a multiscale micromechanical modeling. *Acta Mater.* **59**, 3851–3863 (2011)
31. Zare-Shahabadi, A., Shokuhfar, A., Ebrahimi-Nejad, S., Arjmand, M., Termeh, M.: Modeling the stiffness of polymer/layered silicate nanocomposites: more accurate predictions with consideration of exfoliation ratio as a function of filler content. *Polym. Testing* **30**, 408–414 (2011)
32. Wang, K., Ahzi, S., Matadi Boumbimba, R., Bahlouli, N., Addiego, F., Remond, Y.: Micromechanical modeling of the elastic behavior of polypropylene based organoclay nanocomposites under a wide range of temperatures and strain rates/frequencies. *Mech. Mater.* **64**, 56–68 (2013)
33. Anoukou, K., Zaïri, F., Naït-Abdelaziz, M., Zaoui, A., Qu, Z., Gloaguen, J.M., Lefebvre, J.M.: A micromechanical model taking into account the contribution of α - and γ -crystalline phases in the stiffening of polyamide 6-clay nanocomposites: a closed-formulation including the crystal symmetry. *Compos. B Eng.* **64**, 84–96 (2014)
34. Buckley, C.P., Jones, D.C., Jones, D.P.: Hot-drawing of poly(ethylene terephthalate) under biaxial stress: application of a three-dimensional glass-rubber constitutive model. *Polymer* **37**(2403), 2414 (1996)
35. Adams, A.M., Buckley, C.P., Jones, D.P.: Biaxial hot drawing of poly(ethylene terephthalate): measurements and modelling of strain-stiffening. *Polymer* **41**, 771–786 (2000)
36. Ju, J.W., Sun, L.Z.: Effective elastoplastic behavior of metal matrix composites containing randomly located aligned spheroidal inhomogeneities. Part I: micromechanics-based formulation. *Int. J. Solids Struct.* **38**, 183–201 (2001)
37. Dupaix, R.B., Boyce, M.C.: Constitutive modeling of the finite strain behavior of amorphous polymers in and above the glass transition. *Mech. Mater.* **39**, 39–52 (2007)

38. Doufas, A.K., McHugh, A.J., Miller, C.: Simulation of melt spinning including flow-induced crystallization: Part I. Model development and predictions. *J. Nonnewton. Fluid Mech.* **92**, 27–66 (2000)
39. Ahzi, S., Makradi, A., Gregory, R.V., Edie, D.D.: Modeling of deformation behavior and strain-induced crystallization in poly(ethylene terephthalate) above the glass transition temperature. *Mech. Mater.* **35**, 1139–1148 (2003)
40. Anumula, N., Menary, G., Yan, S., Nixon, J., Martin, P.: Processing - property relations from biaxial deformation of PET (polyethylene terephthalate). *Am. Inst. Phys. AIP Conf. Proc.* **1896**, 060012 (2017)
41. Salem, D.R.: Development of crystalline order during hot-drawing of poly(ethylene terephthalate) film: Influence of strain rate. *Polymer* **33**, 3182–3188 (1992)
42. Wang, Y.H., Wang, W.H., Zhang, Z., Xu, L., Li, P.: Study of the glass transition temperature and the mechanical properties of PET/modified silica nanocomposite by molecular dynamics simulation. *Eur. Polymer J.* **75**, 36–45 (2016)
43. Matsuo, M., Sawatari, C.: Morphological and mechanical properties of Poly(ethylene terephthalate) gel and melt films in terms of the crystal lattice modulus, molecular orientation, and small angle X-ray scattering intensity distribution. *Polym. J.* **22**, 518–538 (1990)
44. Cosson, B., Chevalier, L., Régnier, G.: Simulation of the stretch blow moulding process: from the modelling of the microstructure evolution to the end-use elastic properties of polyethylene terephthalate bottles. *Int.J. Mater. Form.* **5**, 39–53 (2012)
45. Manevitch, O.L., Rutledge, G.C.: Elastic properties of a single lamella of montmorillonite by molecular dynamics simulation. *J. Phys. Chem. B* **108**, 1428–1435 (2004)
46. Figiel, L., Soon, K.H., Buckley, C.P.: Modelling and simulation of the large deformation behaviour of nanoclay/PET nanocomposites near the glass transition. *Model. Simul. Mater. Sci. Eng.* **18**, 015001 (2009)
47. Simo, J.C., Kennedy, J.G., Govindjee, S.: Non-smooth multisurface plasticity and viscoplasticity. Loading/unloading conditions and numerical algorithms. *Int. J. Numer. Methods Eng.* **26**, 2161–2185 (1988)
48. Ju, J.W., Zhang, X.D.: Effective elastoplastic behavior of ductile matrix composites containing randomly located aligned circular fibers. *Int. J. Solids Struct.* **38**, 4045–4069 (2001)

Publisher's Note Springer Nature remains neutral with regard to jurisdictional claims in published maps and institutional affiliations.